European Journal of Mechanics B/Fluids 28 (2009) 494–505

Contents lists available at ScienceDirect

European Journal of Mechanics B/Fluids

www.elsevier.com/locate/ejmflu

The influence of sweep on the linear stability of a series of swept laminar separation bubbles

T. Hetsch [a,*], U. Rist [b]

[a] Aircraft Research Association Ltd, Manton Lane, Bedford, MK41 7PF, UK
[b] Institut für Aerodynamik und Gasdynamik, Universität Stuttgart, Pfaffenwaldring 21, 70550 Stuttgart, Germany

ARTICLE INFO

Article history:
Received 12 April 2008
Received in revised form 16 December 2008
Accepted 5 February 2009
Available online 10 February 2009

Keywords:
Swept laminar separation bubbles
Linear stability theory
Parabolised stability equations
Independence principle

ABSTRACT

The effect of sweep on the linear stability of a series of pressure-induced laminar separation bubbles is investigated for a range of sweep angles $\Psi = 0°$, 15°, 30°, 45° by means of linear stability theory and solutions of the linear parabolised stability equations. An application of the independence principle for infinite swept configurations ensures identical chordwise cross sections of the separation bubbles in the *DNS*-base flows, which enables direct comparisons. Systematic investigations of the local stability and the properties of the linearly most amplified disturbances for each sweep angle show that Tollmien–Schlichting waves, not cross-flow instabilities, dominate even for higher sweep angles. Similar to the situation in attached boundary layers oblique Tollmien–Schlichting waves, which propagate approximately in free stream direction, experience the strongest linear growth in the swept cases. Compared to the strong growth in the separated shear layer, however, their maximum amplification increases only moderately with the sweep angle. The general influence of cross-flow instabilities is weak in the given configuration, despite a relevant cross-flow inside the separation bubble. Finally, the investigation yielded that the comprehensive influence of the independence principle on the base flow is not extendible to the linear stability equations, so that with respect to disturbance amplification in general each sweep angle constitutes a unique case.

1. Introduction

Due to strong adverse pressure gradients and moderate Reynolds numbers, separation bubbles are frequently encountered with high lift devices, near the leading edges of thin profiles, on turbine blades of low pressure gas turbines, blades of wind turbines or in the midsection of laminar airfoils for gliders. The phenomenon occurs in adverse pressure gradient regions, where oncoming laminar boundary layers easily separate from the surface of an aerodynamic body. The strong amplification of boundary layer disturbances in the separated shear layer usually leads to laminar-turbulent transition and the more energetic turbulent boundary layer may then reattach to form a transitional separation bubble, whose global features were described by Gaster [1] and Horton [2]. Laminar boundary layers as in Fig. 1 are typically clearly structured in extended, approximately horizontal layers of comparable velocity and exhibit disturbances which are too small in relation to the base flow velocity profiles to influence them significantly. Turbulent boundary layers on the other hand are characterised by random, three-dimensional, high frequency disturbances with a strong influence on the turbulence mean flow, as they reach amplitudes in the order of 10% of the mean flow profiles.

In low freestream-turbulence environments in combination with sufficiently low Reynolds numbers however, *laminar* reattachment can occur due to a change in the surface geometry or the pressure gradient, giving rise to unsteady laminar separation bubbles with periodic vortex shedding. If the Reynolds number is decreased further, the resulting separation bubbles become completely steady as the present base flow pictured in Fig. 1. Steady laminar separation bubbles have been studied numerically as early as the first conducted direct numerical simulation (*DNS*) of a separation bubble by Briley [3], while a recent investigation of the unsteady case can be found in Castro [4], who investigated the stability of the unsteady flow behind the blunt leading edge of a splitter plate. Experimental realisations of steady and unsteady laminar separation bubbles behind a rounded backward facing step were obtained by Bao [5] in a water towing tunnel. Note that laminar and transitional separation bubbles are often not distinguished in the literature and simply referred to as 'laminar separation bubbles' as opposed to 'turbulent separation bubbles', which separate in turbulent flow.

The prediction of the stability of separation bubbles is a challenging task, because of their complex structure featuring interacting phenomena as flow unsteadyness, separation, backflow and, in

* Corresponding author.
E-mail address: thetsch@ara.co.uk (T. Hetsch).

0997-7546/$ – see front matter
doi:10.1016/j.euromechflu.2009.02.002

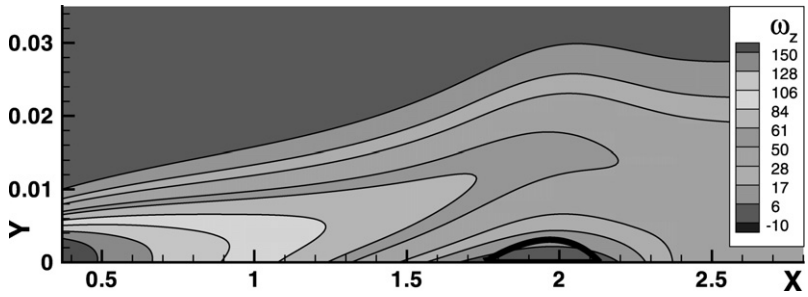

Fig. 1. Sweep angle independent, longitudinal cut through the swept, steady laminar separation bubble of the present *DNS*-base-flow-series. Shown are isolines of the spanwise vorticity ω_z visualising the separated shear layer and additionally the dividing streamline, which forms the outer border of the bubble. The Reynolds number is $Re_{\delta_2}(x_{\text{sep}}) = 330$ based on the momentum thickness at separation.

the case of transitional ones, laminar-turbulent transition. Furthermore, a stability analysis is often hindered by difficulties to define an appropriate unperturbed base flow and due to insufficiencies of available stability theories. Typically the latter are based on linearised equations, but especially in transitional separation bubbles the flow field becomes non-linear when high turbulence levels are reached in the rear part. Therefore, research has focused on idealised, analytical velocity profiles as in the work of Michalke [6], Gaster [7], Allen and Riley [8], Hammond and Redekopp [9] and Alam and Sandham [10]. An important common question in these papers is whether the flow in the separation bubble is absolutely or convectively unstable and whether and where a border between these two regimes can be defined. Interestingly, despite another apparent insufficiency of these earlier approaches, namely neglecting the non-parallelism of the base flow, they were in favourable agreement with direct numerical simulations [10,11] and experimental results [12], which both naturally include the entire flow physics. With the recent emergence of global approaches that solve the stability equations in a two-dimensional domain (in contrast to just a one-dimensional local cut) one limitation of the theory has been overcome and according publications have just appeared, see [13–17], for example. However, even if these techniques have identified additional globally unstable modes, the simpler previous investigations have not been made obsolete so far. The work of Marquet et al. [16], for instance, nicely illustrates that the "amplifier dynamics" (i.e. traditional convective modes) grow much stronger than the "resonator dynamics" (i.e. the globally unstable modes). This proves that classical local linear stability theory is an adequate tool for the small pressure-induced laminar separation bubbles considered here, even after the emergence of more significant tools.

Separation bubbles naturally appear in swept configurations like the transitional bubble detected by Greff [18] on the slat of an Airbus A310 in landing configuration. Despite their practical importance research efforts so far have almost exclusively addressed the unswept case, which does not exhibit cross-flow influences or the sweep angle as an additional parameter and is easier to realise in experiments and simulations. Therefore, literature on swept separation bubbles is rare, predominantly older and often hard to find and obtain, see Hetsch and Rist [19] for a short bibliography.

The reader might want to refer to Horton [2] and Young and Horton [20], who analysed an extensive body of experimental data devoted to swept transitional separation bubbles and to Kaltenbach and Janke [21], Kaltenbach [22] and Jürgens and Kaltenbach [23], who investigated the transitional flow field behind a series of swept, rearward-facing steps by means of *DNS*. This geometry enforces a transitional separation bubble and the effect of sweep was investigated and visualised systematically. Spatial growth rates increased with increasing sweep angle, though Kaltenbach and Janke [21] found only a weak influence. Strong similarities of the laminar shear layer emanating from the step with a free shear layer made linear stability theory for skewed mixing layers as formulated by Lu and Lele [24] applicable. An observed tilting of the rollers associated with the most unstable shear-layer instabilities of Kelvin–Helmholtz type towards smaller angles with respect to the freestream direction, which was between 0°–5°, 10°–20° and 18°–28° for sweep angles of 15°, 30° and 40°, was in good agreement with the "effective shear direction" predicted by that theory. However, a direct transfer of these results to pressure-induced bubbles is unlikely to be accurate, because of known differences of the wall-bounded shear layer of these separation bubbles to free shear layers as discussed by Dovgal, Kozlov and Michalke [25], Rist [26] and Rist, Maucher and Wagner [27]. Therefore, only qualitative guidance can be expected.

As far as separation bubbles on infinite swept configurations are concerned the so-called independence principle provides the key to relate their general topology to the much better understood unswept case. The independence principle of incompressible flow with a homogeneous spanwise direction states that the chordwise cross-section and all flow quantities already present in the unswept case are unaffected by a rising sweep angle, if the chordwise inflow conditions are kept constant. Consequently, swept separation bubbles form leading-edge parallel stream tubes with a spanwise outflow and a helical motion inside as proposed by Horton [2] based on hot-wire measurements for a fixed sweep angle of 26.5°. Exactly these featured were observed by the authors in [19] for sweep angles between 0°–45° based on the same base flow investigated here. Additionally it was shown that the independence principle applies to arbitrary sweep angles below 90° for purely laminar flow fields.

As our knowledge about swept separation bubbles is still quite limited, this study focuses on the open question of the influence of sweep on the linear stability of pressure-induced, swept laminar separation bubbles. The aim is twofold: Firstly, to study the influence of sweep on the local stability as well as on the characteristics of the most amplified disturbances in the given series of laminar separation bubbles systematically. Secondly, to contribute to the investigation of the yet unknown influence of cross-flow instabilities on swept separation bubbles for higher sweep angles. To this end the paper is organised in the following way: After a brief review of the geometry and the employed numerics in Section 2, the properties of the base flow are discussed in Section 3 with emphasis on cross-flow influences. Section 4 contains the main results about the impact of sweep on the linear stability equations and the local flow stability within the separation bubble, as well as an investigation of the associated cross-flow influences in the 45°-case. The paper ends with the conclusions in Section 5.

2. Numerical aspects and employed geometry

The chosen *DNS*-algorithm has evolved over the years and was successfully applied to various transitional flows as for example

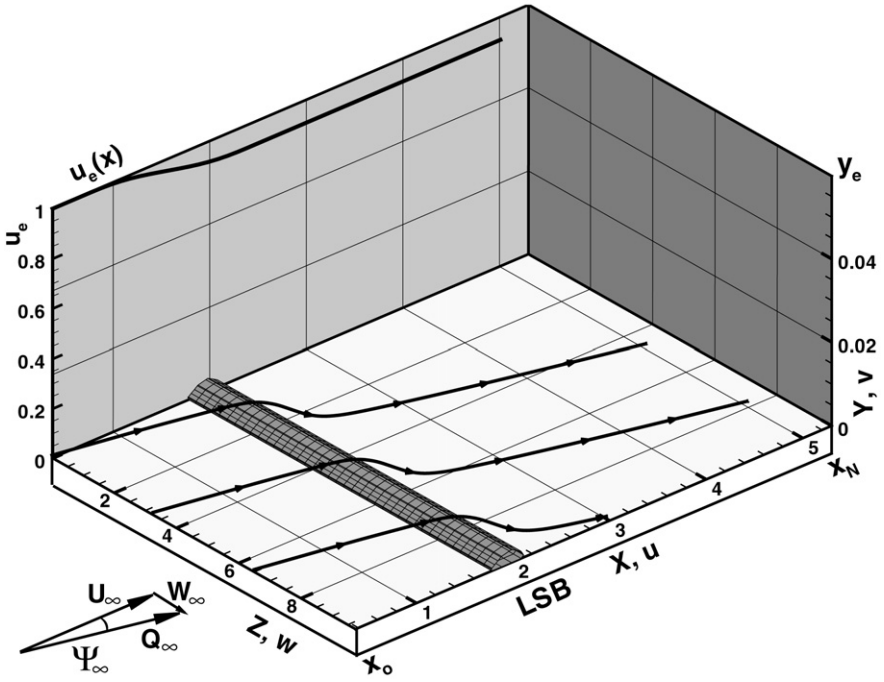

Fig. 2. Calculation domain of the 30°-laminar separation bubble ($x \in [1.75; 2.13]$) with near-wall streamlines over dividing surface $\boldsymbol{\Psi_0}$ from (3). Oncoming flow: Sweep angle Ψ_∞ from (1) and inflow velocity Q_∞ with components U_∞ and W_∞. Velocity distribution $u_e(x)$ of potential flow. The domain starts at $x_o = 0.37$ and extends till $x_N = 5.05$, while its maximum height is reached at $y_e = 0.059 = 18 \cdot \delta_1(x_0)$.

described in Rist and Fasel [28], Bake, Meyer and Rist [29] or Wassermann and Kloker [30]. Typically it was utilised to provide a highly accurate, steady, laminar base flow for unsteady *DNS*-calculations studying the disturbance propagation within this flow. The algorithm discretises the three-dimensional, incompressible Navier–Stokes equations in a velocity–vorticity formulation with central compact finite differences of fourth order in x and y. An initial flow field of Falkner–Skan–Cooke profiles is advanced in pseudo-time until the steady state determined by the boundary conditions is reached. For the present simulations all residuals were smaller then 10^{-10} for the final solution. The laminar DNS-base flow of the present bubble series was resolved with 1394×97 gridpoints in x and y and good spatial resolution was demonstrated in the verification reported by the authors in [31] and [19], which also provide details about the algorithm and the governing equations.

The presented flow field served the authors as a base flow in [32] for an investigation of the interaction of oblique Tollmien–Schlichting waves with swept laminar separation bubbles and in [33] in order to study the transition process in unsteady laminar separation bubbles. All *PSE*-results were obtained by the linear version of the code 'NOLOT' of the DLR-Göttingen. It is described by Hein in [34], where he used the unswept version of the current base flow to prove the applicability of *PSE* to laminar separation bubbles.

In general, the swept, infinite flat plate with a favourable pressure gradient region followed by an adverse one is the most important special case of the 'swept infinite wing'-geometry. It represents the direct numerical analogue of the classical experiments of Gaster [1] and Horton [2], who studied unswept and swept separation bubbles induced by displacement bodies over a flat plate. Due to a constant pressure inflow region in the present study, however, only the decisive adverse pressure gradient region was modelled, which is mandatory to enforce flow separation and allow for the development of the laminar separation bubble series. Such pressure distributions are typical for a flat plate with a rounded backward facing step blending smoothly into another flat plate comparable to the experimental configuration of Bao [5]. While streamline curvature and therefore crossflow influences occur in the vicinity of the separation bubble due to the local pressure rise, these effects are not present in the upstream flow field. This is unlike the situation on a swept wing, where the changeover from a favourable to an adverse pressure gradient leads locally to S-shaped cross-flow profiles (see e.g. Wassermann and Kloker [30], Fig. 3b) in a limited transient region around the maximum thickness of a wing. While the discussed results represent valid DNS-data of swept laminar separation bubbles, the reader should keep in mind that they represent only a first step in the direction of the treatment of swept infinite wings.

The key boundary condition is homogeneity in span, which leads to a quasi-two-dimensional flow field with $w \neq 0$, but $\frac{\partial}{\partial z} = 0$. Fig. 2 gives an overview over the integration domain. Let x, y and z denote the axes in the leading-edge normal, wall normal and spanwise direction and u, v, w and ω_x, ω_y, ω_z the associated velocity and vorticity components, respectively. The inflow velocity Q_∞ can be decomposed into a leading-edge normal component U_∞ and a leading-edge parallel component W_∞ giving rise to a sweep angle

$$\Psi_\infty = \arctan\left(\frac{\bar{W}_\infty}{\bar{U}_\infty}\right) = \arctan(W_\infty) \tag{1}$$

with a bar used to distinguish dimensional quantities throughout the text.

For the independence principle to hold, the Reynolds number based on U_∞ must be kept constant at the value of the unswept case. Thus, all quantities are calculated in a non-dimensional form based on $\bar{U}_\infty = 30$ m/s, a reference length $\bar{L} = 0.05$ m and the kinematic viscosity $\bar{\nu} = 15 \times 10^{-6}$ m^2/s of air resulting in a global Reynolds number of $Re = 100\,000$. As a consequence, the Reynolds number

$$Re_{Q_\infty} = \sqrt{1 + \tan(\Psi_\infty)}\, Re \tag{2}$$

based on the magnitude of the incoming freestream becomes a function of the sweep angle. Keeping Re_{Q_∞} fixed by varying U_∞

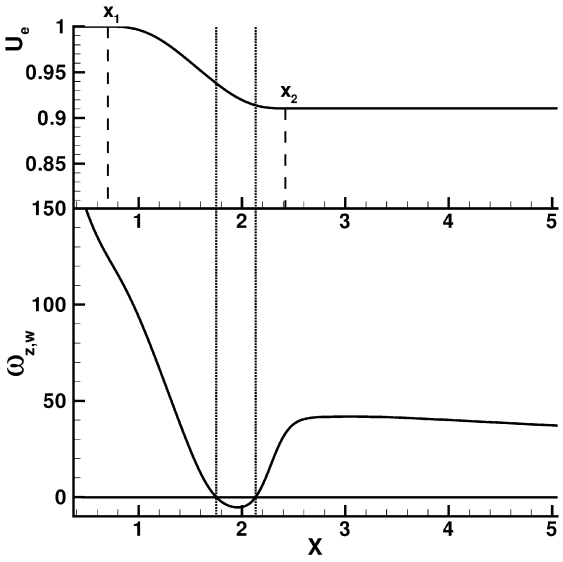

(a) Up: Upper boundary condition consisting of a smooth $u_e(x)$-deceleration of 8.95% U_∞ implemented by a 5th-order polynomial between $x_1 = 0.71$ and $x_2 = 2.42$. The associated pressure rise results in the laminar separation bubble indicated by the spanwise vorticity distribution shown below.

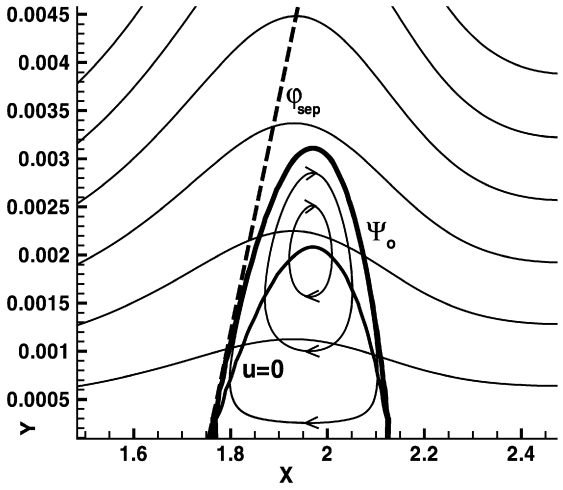

(b) Cross section of 45°-bubble in front of six w-isolines with ascending values between $w = 0.04$ and 0.24. Dividing streamline $\boldsymbol{\Psi_0}$ (3), projection of internal circulation on x–y-plane (closed u–v-streamlines), isoline $u = 0$ and analytical solution of separation angle φ_{sep} after Oswatitsch [39].

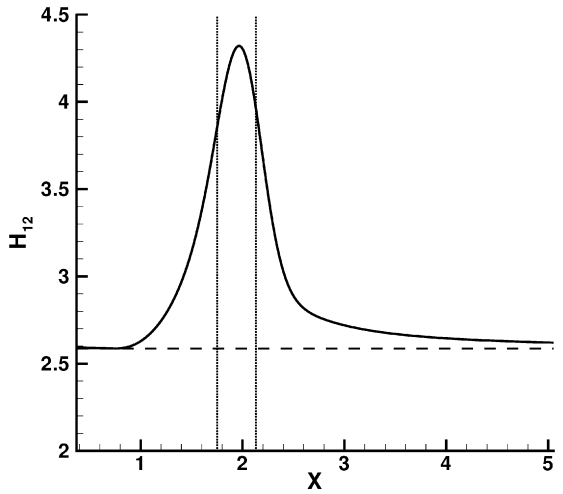

(c) Distribution of the shape factor H_{12}. Horizontal dashed line: typical Blasius value of $H_{12} = 2.59$.

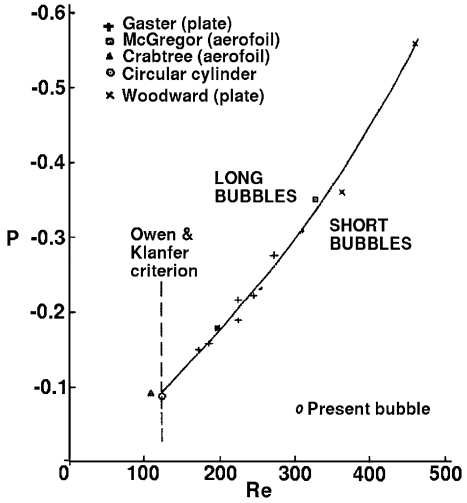

(d) Characterisation of present separation bubble series by comparison to classical experimental results taken from Fig. 1 in Oswatitsch [39]. Axes: Gaster's P-parameter $P = \delta_2^2(x_{sep})/\nu \cdot \Delta u/\Delta x$ (evaluating the average velocity gradient through the bubble at boundary layer edge) over Re_{δ_2}.

Fig. 3. Sweep angle independent base flow parameter of laminar separation bubble series. Their chordwise extent is indicated by vertical, dash-dotted lines at the separation $x_{sep} = 1.75$ and reattachment position $x_{reat} = 2.13$.

would result in increasingly different separation bubbles for higher sweep angles, making a direct comparison less meaningful. The same decision was reached by Kaltenbach and Janke [21].

3. Properties of the separation bubble series and the influence of sweep

The employed separation bubble series is best characterised by the Reynolds numbers $Re_{\delta_1} = \bar{U}_\infty \bar{\delta}_1(x_{sep})/\bar{\nu} = 1271$ and $Re_{\delta_2} = \bar{U}_\infty \bar{\delta}_2(x_{sep})/\bar{\nu} = 330$, based on the displacement thickness δ_1 and the momentum thickness δ_2 at separation. This lies well inside the range of Re_{δ_2} within $\mathcal{O}(10^2)$ to $\mathcal{O}(10^3)$, which is typical for applied configurations like leading edge separation bubbles on thin wings or transitional separation bubbles on high-lift devices as discussed by Alam and Sandham [10]. Likewise, in Table II of [2] Horton calculated values between $Re_{\delta_2} \in [230; 360]$ for his measured swept separation bubble series.

3.1. Characterisation of the separation bubble series through sweep angle independent parameters

The following properties are shared by each of the investigated separation bubbles, as they are sweep angle independent by virtue of the independence principle. Under the influence of the decelerating chordwise potential velocity distribution $u_e(x)$ depicted in Fig. 3(a) the flow separates at $x_{sep} = 1.75$ and reattaches in a laminar flow regime at $x_{reat} = 2.13$ as visualised in Fig. 1. In between a laminar separation bubble is formed, as indicated in Fig. 3(a)

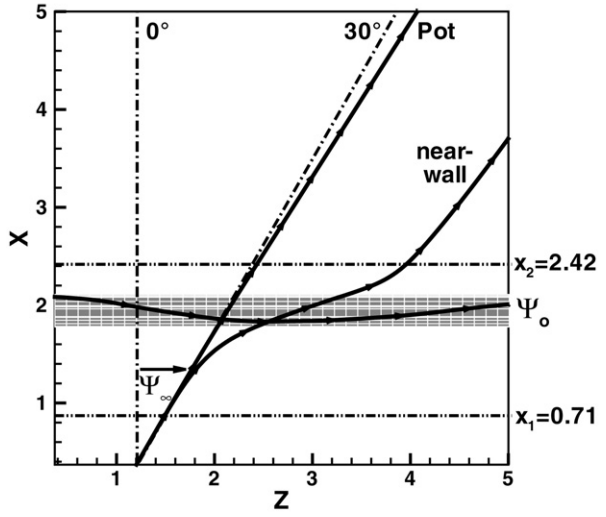

(a) Topview on dividing streamsurface Ψ_0 of 30°-bubble: Bending of potential streamline ("Pot") caused by u_e-deceleration between $x_1 = 0.71$ and $x_2 = 2.42$, in comparison to skewed near-wall streamline, sweep angle $\Psi_\infty = 30°$ (dash-dotted) and straight potential streamline (dashed) obtained for $\Psi_\infty = 0°$. Helical streamline inside bubble indicates noticeable spanwise velocity there.

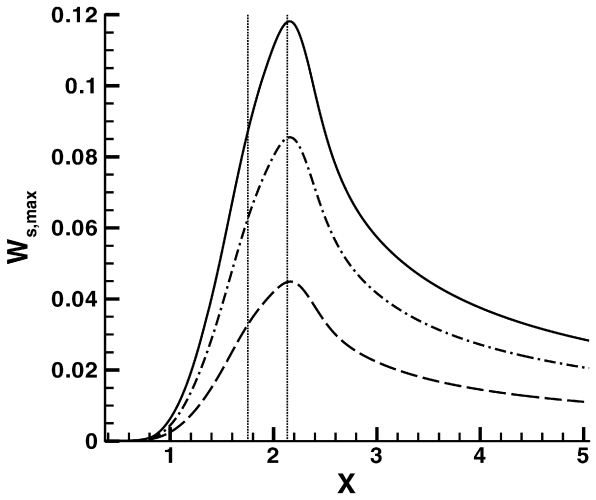

(b) Strength of maximal cross-flow component $w_{s,\max}(x) = \max_y(w_s(x, y))$ along chord with respect to U_∞ for $\Psi_\infty = 45°$ (line), 30° (dash-dotted), 15° (dashed). No cross-flow in unswept $\Psi_\infty = 0°$ case.

Fig. 4. Influence of rising sweep angle on present laminar separation bubble series.

by the spanwise wall vorticity distribution $\omega_{z,w}$, which is directly proportional to the wall shear stress $\bar{\tau}_x = \bar{\mu}(\frac{\partial \bar{u}}{\partial \bar{y}})|_w = \bar{\mu}\bar{\omega}_z|_w$ and thus shows the characteristic negative wall shear stress due to the backflow inside. As shown in Fig. 3(b) its outer shape is best visualised by means of the separated wall-streamline calculated from the two-dimensional streamfunction

$$\boldsymbol{\Psi_0} := \big\{(x, y) \mid \boldsymbol{\Psi}(x, y) = 0\big\}, \quad \text{with } \boldsymbol{\Psi}(x, y) := \int_0^{y_e} u(x, y)\, dy. \tag{3}$$

Exploiting the homogeneity of the base flow in span, this defines a "dividing surface" of constant cross section. The inflow located at $x_o = 0.37$ is governed by zero pressure gradient Falkner–Skan–Cooke profiles and $Re_{\delta_1}(x_o) = 331$. The domain extends 12 bubble lengths in chordwise direction to $x_N = 5.05$, while the wall normal coordinate $y_e = 0.06$ at the upper domain edge corresponds to 19 separation bubble heights. The ratio of the separation bubble length $L_{\mathrm{LSB}} = 0.38$ to the boundary layer thickness at separation $\delta_{99}(x_{\mathrm{sep}}) = 0.027$ is 14 : 1.

The presence of a separation bubble deforms the local displacement and momentum thicknesses leading to the steep rise and fall of the shape factor $H_{12} = \delta_1/\delta_2$, as demonstrated in Fig. 3(c). Due to the free-stream velocity distribution from Fig. 3(a) it increases from a characteristic Blasius value of $H_{12} = 2.59$ to a maximum of $H_{12} = 4.32$ in the middle of the separation bubble. Separation here occurs at $H_{12} = 3.85$ slightly below the theoretical value of $H_{12} \approx 4$ which is obtained for a self-similar Falkner–Skan boundary layer. Note the persistent downstream influence of the separation bubble as H_{12} approaches 2.59 asymptotically in the zero-pressure-gradient region of the domain outflow region without reaching it.

Finally, a direct comparison of the present separation bubble series with classical experimental results in Fig. 3(d) shows that we are dealing with "short" separation bubbles far from any disposition to bursting. Test-simulations with unsteady disturbance generation in front of the separation bubble in connection with [32] confirmed the convectively unstable character of this configuration.

3.2. Effects of a rising sweep angle: Streamline bending, spanwise velocity and cross-flow influences

The introduction of a sweep angle causes a streamline-bending, which is not present in the unswept case, as Fig. 4(a) illustrates for the 30°-bubble. From the definition of the direction of the potential streamline

$$\Psi_e(x) = \arctan\big(W_\infty/u_e(x)\big) \tag{4}$$

and the monotony of the arctan-function it is clear that the straight streamlines of the zero-pressure gradient inflow zone must bend to the right in Fig. 4(a) under the influence of the freestream deceleration of Fig. 3(a). Following a qualitative argument from Horton [2] we can expect a crosswise pressure gradient

$$\frac{\partial p}{\partial n} = -\frac{\rho u_e^2}{R}$$

to act on the curved external streamlines, if R denotes the radius of curvature and n the direction normal to the streamline and outwards from the centre of curvature. As the static pressure is constant throughout the boundary layer within the accuracy of the boundary layer equations, while the flow increasingly decelerates towards the wall due to friction, the local radius of curvature must decrease fast in order to keep the balance of forces. Thus, near-wall streamlines must turn inwards towards the centre of curvature of the potential streamline, as can be observed from Fig. 4(a). This gives rise to a so-called "secondary flow", which expresses itself in a crossflow component w_s at right angle to the streamwise velocity component u_s in the local direction of the potential flow

$$\begin{aligned} u_s &= \cos(\Psi_e) \cdot u + \sin(\Psi_e) \cdot w, \\ w_s &= -\sin(\Psi_e) \cdot u + \cos(\Psi_e) \cdot w, \end{aligned} \tag{5}$$

which are the natural velocity components along the local x_s and z_s-directions of a streamline-oriented coordinate system. Quantities in this system are here denoted with a subscript "s". For disturbance waves the same transformation can be applied to the wave numbers $\alpha_r = \bar{\alpha}_r \bar{L}$ and $\gamma = \bar{\gamma}\bar{L}$ in x and z in order to obtain the corresponding wave numbers in x_s and z_s

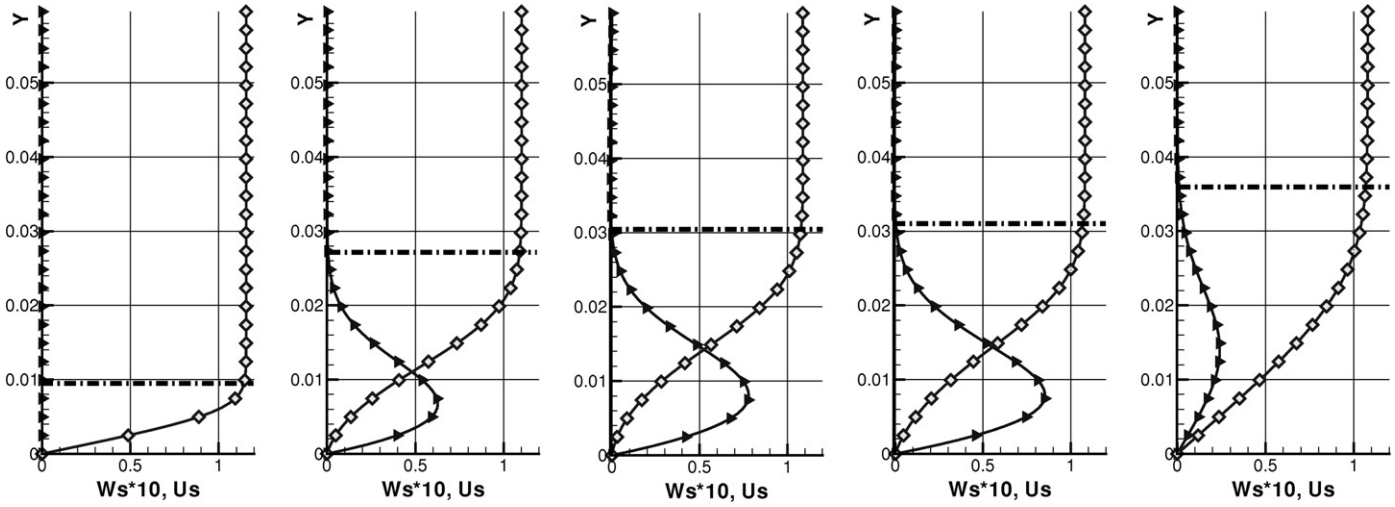

Fig. 5. Streamwise and cross-flow velocity profiles from (5) for 30°-base flow at significant x-positions: Inflow ($x_o = 0.37$), separation ($x_{sep} = 1.75$), middle of separation bubble ($x = 1.96$), reattachment ($x_{reat} = 2.13$) and six bubble length downstream of reattachment ($x = 4.4$). Symbols: $u_s(y)$ (diamond), $w_s(y)$ (triangle). Dash-dotted, horizontal line: $\delta_{99,s}$ based on u_s.

$$\alpha_{r,s} = \cos(\Psi_e)\cdot\alpha_r + \sin(\Psi_e)\cdot\gamma,$$
$$\gamma_s = -\sin(\Psi_e)\cdot\alpha_r + \cos(\Psi_e)\cdot\gamma, \tag{6}$$

which was utilised to transform the linear stability results of the swept base flows into the streamline-oriented, physically relevant $\alpha_{r,s}$–γ_s-system in Section 4.

As an overview, Fig. 5 shows the downstream development of u_s and w_s for $\Psi = 30°$: While no crossflow is present at the inflow due to the missing curvature of the local potential streamline, a strong crossflow-component w_s is induced by the local u_e-deceleration within the bubble. In the out-flow region the flow is asymptotically approaching Falkner–Skan–Cooke-characteristics again, but a weak crossflow is still persistent. The presence of inflection points in the cross-flow profiles displayed in Fig. 5 gives rise to an inviscid cross-flow instability, whose strength is investigated by means of linear stability theory and *PSE* in Section 4.

The cross-flow levels of the present flow documented in Fig. 4(b) are comparable to values reported for swept boundary layers in the literature: Relative to the inflow velocity U_∞ the maximum cross-flow velocity $w_{s,\max}(x) = \max_y(w_s(x,y))$ rises to a maximum of 12% for the 45°-case and decreases to 3% towards the outflow. For a sweep angle of $\Psi_\infty = 30°$ one observes about 9% and 2%, respectively. Chernoray et al. [35] measured a monotonously decreasing cross-flow component between 10% at the beginning of the pressure drop and 3% at 80% chord of a model of a C-16 wing for $\Psi_\infty = 30°$ and $\bar{U}_\infty = 12.8$ m/s. With respect to the local streamwise freestream component $u_{s,e}$ the shape of the distribution in Fig. 4(b) stays the same, but the maximal value decreases to 9% for $\Psi_\infty = 45°$, to 8% for 30° and to 5% for 15°.

Fig. 4(a) shows a helical motion of the streamlines within the separation bubble, which indicates the presence of a significant spanwise velocity component w. Indeed, contours of w exhibit a local maximum in the vicinity of the separation bubble as demonstrated in Fig. 3(b), where w reaches a maximum of 11% U_∞ inside at the tip of the 45°-bubble. For smaller sweep angles the strength of this spanwise flow decreases with the tangent of Ψ_∞, as the entire laminar flow field may be obtained analytically by scaling

$$u = u_{45°}, \quad v = v_{45°}, \quad \omega_z = \omega_{z,45°}; \quad w = \tan(\Psi_\infty)w_{45°},$$
$$\omega_x = \tan(\Psi_\infty)\omega_{x,45°}, \quad \omega_y = \tan(\Psi_\infty)\omega_{y,45°} \tag{7}$$

of the generic 45°-case due to the infinite swept geometry as derived in Hetsch and Rist [19] or [31].

4. The influence of sweep on the linear stability of the laminar separation bubble series

In order to provide a first overview about spatial linear stability properties of swept laminar separation bubbles, the neutral stability surface of the 30°-case is shown in Fig. 6(a) as a function of the three-dimensional parameter space (x, ω, γ_s), where $\omega = 2\pi f$ denotes the angular frequency of the analysed disturbance wave. As with all data throughout the study, frequencies $f = \bar{f}\bar{L}/\bar{U}_\infty$ are non-dimensionalised with the reference quantities given at the end of Section 2. The presence of the laminar separation bubble in combination with the generating adverse pressure gradient has a noticeable impact on the local flow stability: Fig. 6(b) compares the stability of this flow with the stability of the flow field under the same inflow conditions, but with zero pressure gradient. For the comparison Tollmien–Schlichting-waves (*TS*) with a spanwise wave number of $\gamma = 0$ and thus leading-edge parallel wave fronts have been chosen due to their importance to the unswept reference case and because they are the only one whose amplification is sweep-angle independent, so that this particular stability diagram is characteristic for all four considered base flows. Their maximal amplification rate increases 16 times from $\alpha_i = -0.74$ to -11.99 inside the bubble, a much broader frequency spectrum of disturbances is amplified and x_{crit}, the point where the unswept base flow first becomes unstable in accordance with the Squire theorem, is shifted upstream from 0.95 to 0.81. Note that the Squire theorem, predicting earliest amplification for $\gamma = 0$, is only concerned with unswept base flows. For the 30°-base flow in Fig. 8(a) for example earliest amplification occurs around $\gamma_s = 0$ and thus for disturbance waves which are "two-dimensional" within the local streamline-oriented coordinate system and propagate in the direction of the oblique inflow. The comparison in Fig. 6(b) also shows that the flow reapproaches the characteristics of a zero-pressure gradient boundary layer flow downstream of a transient region of about two to three bubble lengths after reattachment.

Hein [34] performed a *PSE*-calculation of the analogue to the lower stability diagram in Fig. 6(b) based on data of the corresponding unswept case by Rist and Maucher [36]. A comparison of Fig. 2 in [34] indicates that there is no noticeable difference between a PSE-based stability diagram and the present LST-based stability diagram, such that stability diagrams, which usually provide a visual, qualitative overview, may be based on LST throughout the text.

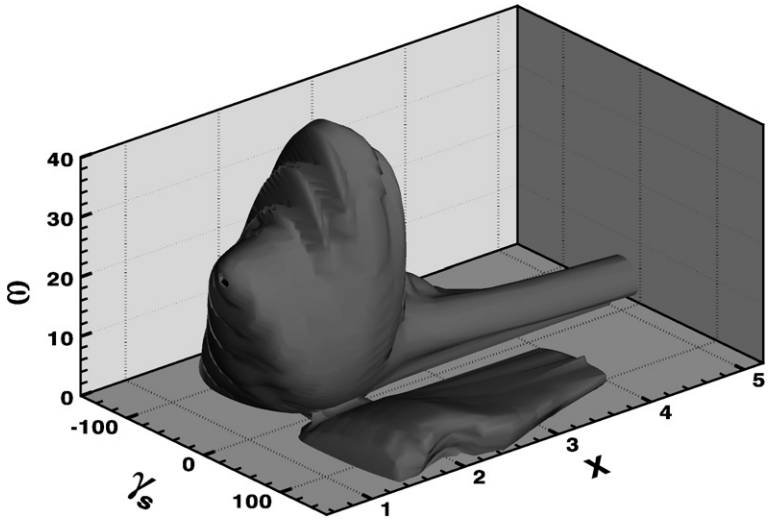

(a) Isosurface of neutral stability $\alpha_i = 0$ of chordwise amplification α_i. Disturbance amplification for combinations of chordwise position x, angular frequency ω, spanwise wave number γ_s inside.

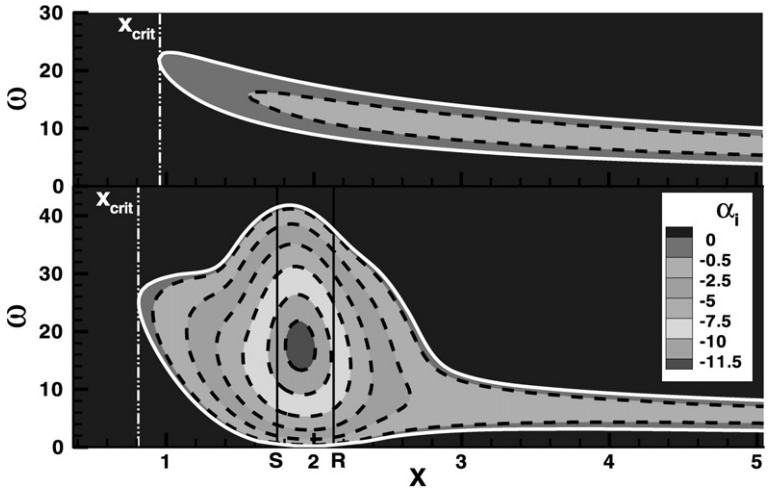

(b) Comparison of stability diagram of bubble (below) with swept zero pressure-gradient flow (above) developing under identical inflow conditions, but without the free-stream deceleration from Fig. 3(a) for $\gamma = 0$. Note upstream shift of point x_{crit} of earliest disturbance amplification in unswept base flow. *S*: Separation position $x_{sep} = 1.75$, *R*: Reattachment position $x_{reat} = 2.13$.

Fig. 6. Linear stability diagrams of separation bubble for sweep angle $\Psi_\infty = 30°$ based on *LST*.

4.1. The impact of sweep on the linear stability equations

As the independence principle provides a complete analysis of the effect of sweep on the base flow structure by virtue of (7), one has to check whether these scaling rules may be extended to the linear stability theory analysis of incompressible flow with a homogeneous spanwise direction, at least for special cases. Inserting (7) in the Orr–Sommerfeld equation and the Squire equation as implemented in the utilised linear stability solver demonstrates that this is not the case in general: a rising sweep angle Ψ_∞ just increases the influence of the $w_{45°}$-profile relative to the u-profile, which are both sweep angle independent.

$$\begin{aligned}
&\frac{\partial^4 \hat{v}'}{\partial y^4} - 2\left(\alpha^2+\gamma^2\right)\frac{\partial^2 \hat{v}'}{\partial y^2} + \left(\alpha^2+\gamma^2\right)\hat{v}' \\
&\quad - iRe\Big\{\left(\alpha u + \gamma \tan(\Psi_\infty) w_{45°} - \omega\right) \\
&\quad \times \left(\frac{\partial^2 \hat{v}'}{\partial y^2} - \left(\alpha^2+\gamma^2\right)\hat{v}'\right) \\
&\quad - \left(\alpha \frac{\partial^2 u}{\partial y^2} + \gamma \tan(\Psi_\infty)\frac{\partial^2 w_{45°}}{\partial y^2}\right)\hat{v}'\Big\} = 0, \qquad (8)
\end{aligned}$$

$$\begin{aligned}
&i\left(\alpha^2+\gamma^2\right)\frac{\partial^2 \hat{u}'}{\partial y^2} + \alpha \frac{\partial^3 \hat{v}'}{\partial y^3} \\
&\quad - \left(\left(\alpha^2+\gamma^2\right) + iRe\left(\alpha u + \gamma \tan(\Psi_\infty) w_{45°} - \omega\right)\right) \\
&\quad \times \left(i\left(\alpha^2+\gamma^2\right)\hat{u}' + \alpha \frac{\partial \hat{v}'}{\partial y}\right) \\
&\quad - iRe\left(\gamma^2 \frac{\partial u}{\partial y} - \alpha\gamma \tan(\Psi_\infty)\frac{\partial w_{45°}}{\partial y}\right)\hat{v}' = 0. \qquad (9)
\end{aligned}$$

Here $\hat{v}'(y)$ denotes the eigenfunction of the wall normal disturbance velocity distribution of a plane travelling disturbance wave and $\hat{u}'(y)$ the correspondent chordwise disturbance velocity profile, while i refers to the imaginary unit. However, as the spanwise velocity w always appears with a factor γ in (8) and (9) at least for leading-edge parallel disturbances with $\gamma = 0$ the stability analysis becomes sweep angle independent. Thus a stability diagram analogue to Fig. 6(b) of the unswept case readily provided starting points for the swept cases, when a shooting method was

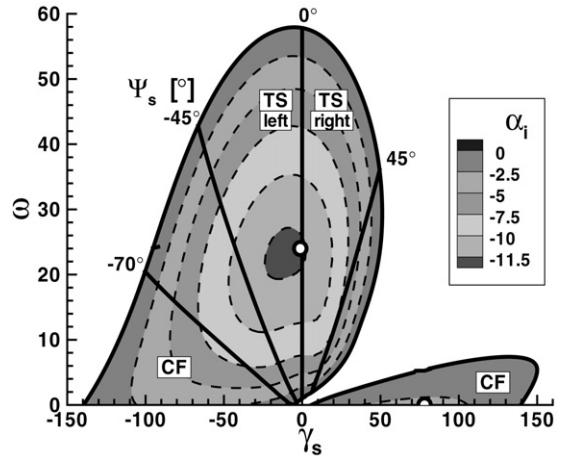

(a) $\Psi_\infty = 45°$: Isolines of propagation direction Ψ_s in front of contours of amplification rate α_i. Circles: location of globally most amplified *TS*-wave $(\omega/\gamma) = (24/30)$ and *CF*-vortex (0/50).

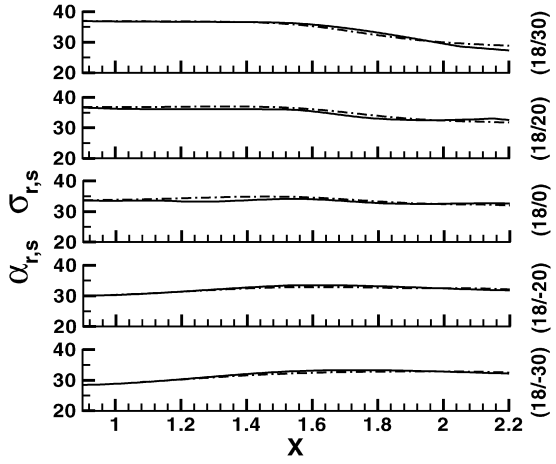

(b) $\Psi_\infty = 45°$: Streamwise wave numbers $\alpha_{r,s}$ from *LST* (dash-dot), $\sigma_{i,s}$ from *PSE* (line) in 45°-separation bubble for disturbance waves (ω/γ) with different propagation directions.

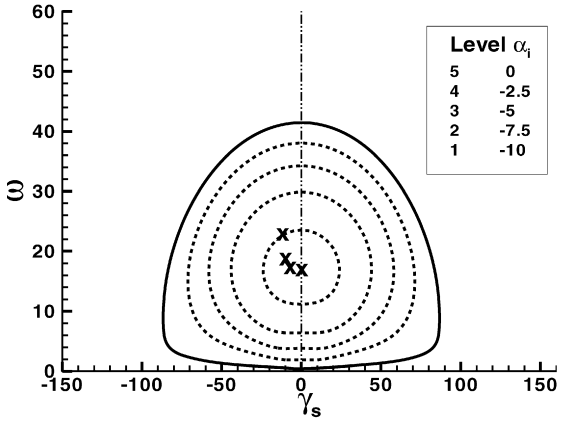

(c) Stability diagram for unswept case $\Psi_\infty = 0°$. "X" marks shift in location of local amplification maximum for $\Psi_\infty = 0°, 15°, 30°, 45°$ (r. to l.).

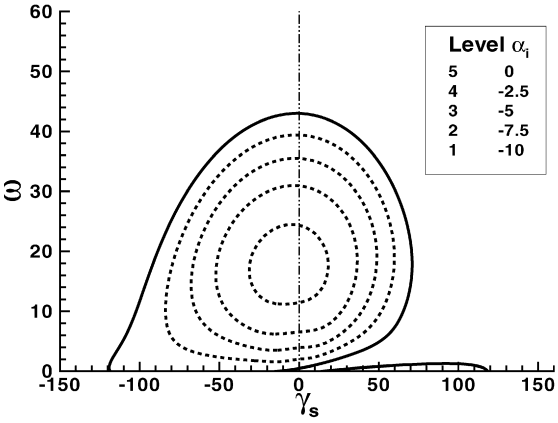

(d) Stability diagram for $\Psi_\infty = 15°$. Amplification of steady cross-flow vortices with $\omega = 0$ for separation bubbles with a sweep angle $\Psi_\infty > 0$.

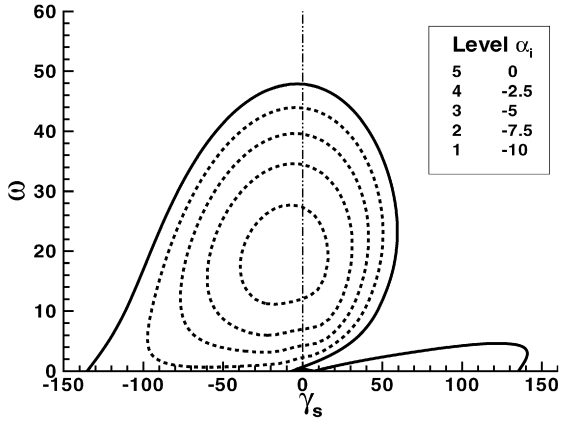

(e) Stability diagram for $\Psi_\infty = 30°$.

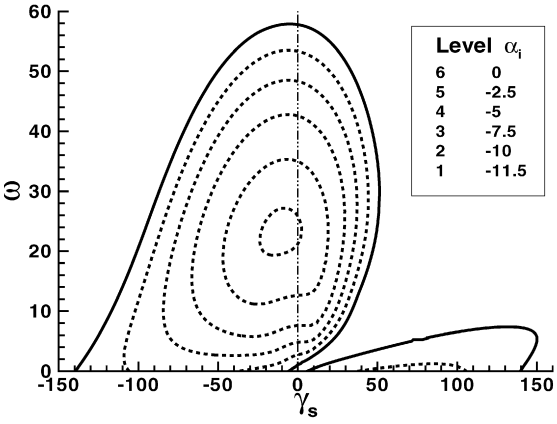

(f) Stability diagram for $\Psi_\infty = 45°$.

Fig. 7. Linear stability results. Fig. 7(b) compares the chordwise wave number in the vicinity of the separation bubble as determined by *LST* and *PSE*. All other figures show the effect of an increasing sweep angle Ψ_∞ on the local *LST*-amplification rate α_i at the separation position $x_{sep} = 1.75$. The outer contour represents the isoline of neutral stability $\alpha_i = 0$.

employed to obtain the *LST*-results for the presented separation bubble series.

4.2. The effect of sweep on the local stability within the separation bubble

The stability diagrams of Fig. 7 exemplify the situation at the separation point, but qualitatively comparable visualisations may be obtained at any chordwise position within the separation bubble. We are interested in the effect of sweep on the local stability of the flow with respect to Tollmien–Schlichting (*TS*) and crossflow-instabilities (*CF*). Fig. 7(a) provides a first, rough overview over their relative strengths and positions in the 45°-base flow. In contrast to *TS*-waves, which typically propagate approximately in the direction of the outer streamline, *CF*-modes exhibit by definition wave vectors which are oriented nearly per-

Table 1
Local parameters of most amplified disturbances (ω/γ) at $x_{sep} = 1.75$ for all sweep angles Ψ_∞ obtained by *LST*: maximal spatial amplification rate $-\alpha_{i_{max}}$, frequency ω, spanwise wavenumber γ, wavenumbers $\alpha_{r,s}$ and γ_s (6), propagation direction $\Psi = \Psi_e + \Psi_s$ with respect to x-axis, free-stream direction Ψ_e (4) and propagation direction Ψ_s (10). Reynolds number Re_{Q_∞} based on total velocity Q_∞ of oncoming flow: effect of increase in Q_∞ via (2), while $Re = Re_{U_\infty} = 100{,}000$ is constant.

Ψ_∞	$-\alpha_{i_{max}}$	ω	γ	$\alpha_{r,s}$	γ_s	Ψ	Ψ_e	Ψ_s	Re_{Q_∞}
0°	10.89	17.17	0.00	47.32	0.00	0.0°	0.0°	0.0°	100,000
15°	10.95	17.53	5.76	46.34	−7.21	7.1°	15.9°	−8.8°	103,533
30°	11.17	18.99	14.43	43.96	−10.10	18.7°	31.6°	−12.9°	115,467
45°	11.68	23.12	22.50	42.00	−11.86	31.0°	46.8°	−15.8°	141,433

pendicular to the potential flow. As the relevant reference direction in a three-dimensional boundary layer is given by the local free stream angle Ψ_e, it is beneficial to switch to the streamline-oriented coordinate system. This allows to distinguish left and right running modes with respect to Ψ_e by means of the propagation direction

$$\Psi_s = \arctan(\gamma_s/\alpha_{r,s}). \tag{10}$$

Nevertheless, as the spanwise wave number γ and the frequency ω of a disturbance wave in a homogeneous medium stay globally constant in a swept infinite geometry while γ_s is a function of x, the pair (ω/γ) is used to identify a particular disturbance from now on.

Systematic evaluations of disturbance waves as in Fig. 7(b) showed consistently that the spatial linear stability theory is very accurate in predicting the chordwise wave number α_r and thus its streamwise counterpart $\alpha_{r,s}$ even for very oblique waves and large sweep angles. Thus, parameters of disturbance waves which are based on wave numbers, such as their propagation direction, but also the wavelength $\lambda = \bar{\lambda}/\bar{L}$ and phase speed $c_r = \bar{c}_r/\bar{U}_\infty$ in propagation direction

$$\lambda = 2\pi/\sqrt{\alpha_{r,s}^2 + \gamma_s^2}, \qquad c_r = \omega/\sqrt{\alpha_{r,s}^2 + \gamma_s^2}, \tag{11}$$

were determined by means of *LST* throughout the study.

With a rising sweep angle Ψ_∞ the initially symmetrical stability diagram becomes increasingly distorted and the amplification maximum moves to oblique waves with negative γ_s and higher frequencies as marked in Fig. 7(c). Table 1 shows that left-running Tollmien–Schlichting waves with a propagation direction of approximately $\Psi_s = -10°$ experience the strongest local amplification even for the higher sweep angles. At the separation point the maximal amplification for $\Psi = 45°$ is 7% higher than in the unswept 0°-case. This trend increases further, but moderately inside the bubble. In the front part at $x = 1.85$, for example, the maximal local amplification of the 45°-case is 8.5% stronger. At the same time, however, the Reynolds number Re_{Q_∞} based on total velocity Q_∞ of the oncoming flow has increased from 100,000 for $\Psi_\infty = 0°$ to 141,433 for $\Psi_\infty = 45°$, so that in addition to changed stability characteristics due to the swept inflow a more unstable flow is to be expected as a result of our chosen model and Eq. (2). Two-dimensional cuts such as Fig. 7(e) through different planes of the three-dimensional x-omega-gammas-space as e.g. visualized in Fig. 6(a) confirm the existence of a unique global maximum for each sweep angle. From there the amplification rates decrease monotonously in all directions towards the surface of neutral stability. As gradients are small the dependency on the frequency ω and on the spanwise wave number γ is weak and moderate changes in either of them have only slight effects on the global amplification of the corresponding modes.

4.3. Identification and properties of the most amplified TS-wave for each sweep angle

From the viewpoint of laminar-turbulent transition the global linear amplification of disturbance waves in the separation bubbles are of interest, as indicated by the amplification curves $A_n e^{N(x)}$. Here A_n denotes the initial amplitude of the disturbance wave at the neutral point x_n and N the so-called N-factor of the integrated local amplification rates α_i or the local *PSE*-amplification rate σ_r as defined in Section III.A in [40] based on the u-disturbance velocity:

$$\begin{aligned} &LST: \quad N(x) = \int_{x_n}^{x} -\alpha_i(\tilde{x})\, d\tilde{x}, \\ &PSE: \quad N(x) = \int_{x_n}^{x} -\sigma_r(\tilde{x})\, d\tilde{x}. \end{aligned} \tag{12}$$

The linearly most amplified *TS*-waves are probable candidates to trigger transition in a scenario with a broad spectrum of disturbance modes of small and comparable initial amplitudes. Naturally, the identified modes may depend to some degree on the x-position at which the comparison is made. The location of the maximum N-factor within the flow field varies from mode to mode and occurs about one bubble length downstream of the region of interest, the separation bubble. Neither is the reattachment point a good choice, as the local flow will typically be in the late non-linear stages of transition already under the influence of small boundary layer disturbances, leading to an unsteady, swept laminar separation bubble with vortex shedding, as studied in Hetsch and Rist [33]. Even for a fixed configuration the end of the linear domain still depends on the initial disturbance spectrum beyond the scope of the linear theories employed here. But investigations by Marxen, Lang, Rist and Wagner [12] demonstrate a good agreement of u- and v-velocity profiles obtained experimentally, by linear stability theory, and from a DNS up to the middle of an unswept transitional separation bubble for realistic initial amplitudes despite strong amplification in the separated shear layer. Therefore, the middle of the separation bubbles at $x = 1.94$ was chosen. Other positions in the front part of the separation bubble would lead to modes with identical or nearly the same frequency ω and spanwise wave number γ, which would not effect the conclusions due to the weak dependence of the linear amplification on ω and γ found in Subsection 4.2.

We note in passing that the *time mean* of the *DNS*-results, which naturally includes the mean-flow distortion of the disturbance background, was utilised as a base flow for the successful comparison in [12]. This is of cause only possible in an *a posteriori*-analysis as in [12], to aid the interpretation of the *DNS*-results. Otherwise, any linear analysis in transitional separation bubbles should be conducted with caution due to the unknown non-linear upstream effect of the mean-flow disturbance generated by the high disturbance levels in the transitional rear part, that could not been calculated even by non-linear *PSE* due to its parabolic character.

Due to the monotonous decline of the local amplification rate from a unique maximum for each x it was sufficient to consider the parameter subspace $x \in [0.9; 1.94]$, $\omega \in [15; 30]$ and $\gamma \in [0; 30]$ around curves of maximal local amplification as the one displayed in Fig. 8(a). The results based on systematic comparisons of *LST*-amplification curves within the search region are compiled in Table 2 and visualised in Fig. 8(b). Typical values of local wave properties could be based on the streamwise wave number $\alpha_{r,s}$ at the separation point, as checks like Fig. 7(b) demonstrate that $\alpha_{r,s}$ changes only slowly with x in the present flow.

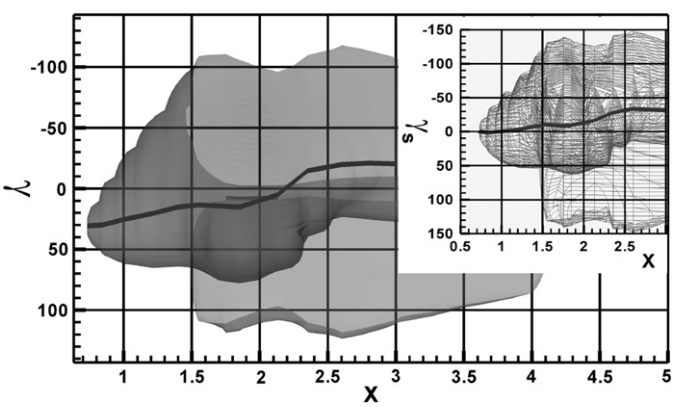

(a) Top-view on the *LST*-stability diagram of the 30°-separation bubble in Fig. 6(a), but in body-oriented x–γ-coordinate system: isosurface of neutral stability $\alpha_i = 0$ with line of maximal local amplification inside. Insert: close-up of surface mesh of region around neutral point in the streamline-oriented x–γ_s-coordinate system.

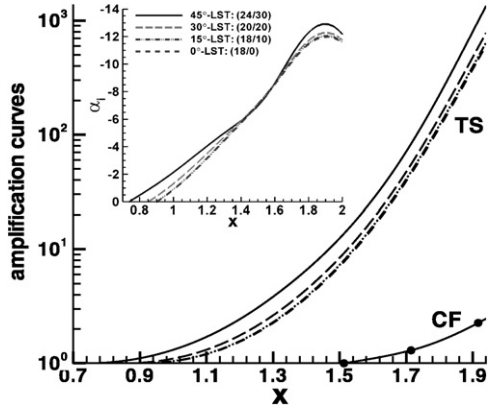

(b) Growth of most amplified *TS*-waves 45°–(24/30) (line), 30°–(20/20) (long dashed), 15°–(18/10) (dash-dotted), 0°–(18/0) (dashed), *CF*-vortex 45°–(0/50) from neutral point to the middle of the bubble. *TS*-wave growth from *LST*, *CF*-vortex from *PSE*. Insert: amplification rates α_i of same *TS*-waves from *LST*.

Fig. 8. Identification of linearly most amplified modes (ω/γ) for each sweep angle.

Table 2
Parameters of globally most amplified *TS*-waves from neutral point x_n to middle of separation bubble $x_m = 1.94$ for all sweep angles Ψ_∞ obtained by *LST*: angular frequency ω, spanwise wavenumber γ, amplitude gain amp with respect to initial amplitude $\text{amp}(x_n) = 1$, N-factor. Typical local parameter at separation point $x_{sep} = 1.75$: free-stream direction Ψ_e (4), propagation direction $\Psi = \Psi_e + \Psi_s$ in body-fitted coordinate system and Ψ_s (10), phase speed c_r and wave length λ from (11).

Ψ_∞	(ω/γ)	Ψ_e	Ψ	Ψ_s	c_r	λ	x_n	amp(x_m)	$N(x_m)$
0°	(18/0)	0°	0°	0°	0.37	0.128	0.91	605	6.4
15°	(18/10)	15.9°	12.1°	−3.8°	0.38	0.133	0.91	640	6.5
30°	(20/20)	31.6°	25.9°	−5.7°	0.44	0.137	0.86	780	6.7
45°	(24/30)	46.8°	44.6°	−2.2°	0.56	0.147	0.75	1340	7.2

Table 3
Maximal local amplification rates $\alpha_{i,\max}[(0/\gamma)]$ of steady cross-flow vortices with corresponding spanwise wave number γ at several chordwise positions around the 45°-bubble between $x_{sep} = 1.75$ and $x_{reat} = 2.13$ according to *LST*. Contrasted with amplification rates $\alpha_{i,\max}[TS]$ of local most amplified *TS*-wave. Last row: percentage of *CF*- to *TS*-amplification.

45°-bubble	$x = 1.0$	$x = 1.4$	$x = 1.75$	$x = 1.85$	$x = 2.13$	$x = 2.36$	$x = 4.5$
$\alpha_{i,\max}[(0/\gamma)]$	> 1	−0.10	−3.16	−3.69	−4.08	−3.00	−0.38
$\pm\gamma\,(\alpha_{i,\max})$	–	55	46	45	40	46	39
$\alpha_{i,\max}[TS]$	−2.33	−6.38	−11.68	−12.84	−9.85	−6.14	−1.23
CF: % of *TS*	–	1.6%	27%	29%	41%	49%	31%

Table 2 shows that oblique, left-running *TS*-waves close to the local freestream direction are the linearly most amplified disturbance modes. The deviation Ψ_s from the freestream direction increases from 0° in the unswept separation bubble to a maximum of about −6° in the 30°-case. Due to a monotonous decline of $\alpha_{r,s}$ as opposed to the frequency a significant rise in the phase speed with the sweep angle is observed, accompanied by a rising wave length. For all four sweep angles Fig. 8(b) shows that *TS*-waves experience a maximal linear growth of roughly three orders of magnitudes from the neutral point to the middle of the separation bubble. There, the most amplified mode within the 45°-separation bubble reaches about twice the amplitude of the corresponding *TS*-wave of the unswept case. This raises the question whether the increase is mainly due to an upstream movement of the neutral point from $x_n = 0.91$ (for $\Psi_\infty = 0°$) to $x_n = 0.75$ (for $\Psi_\infty = 45°$), a shift of 18% of the former value. The insert in Fig. 8(b) displaying the distribution of the local amplification rates confirms that the *TS*-waves exhibit not only earlier, but additionally almost everywhere stronger amplification with rising sweep angle. Both effects are due to three interconnected reasons: the increasing influence of the spanwise velocity w on the linear stability equations as discussed in Subsection 4.1, the simultaneous increase in Re_{Q_∞} due to (2) as discussed in Subsection 4.2 and due to the comparison of different modes in base flows with different sweep angles.

4.4. Cross-flow influences on the investigated separation bubble series

A major difference of swept laminar separation bubbles in comparison to the unswept case is the occurrence of cross-flow disturbances with an unknown influence on the transition process. Thus, the aim is to determine the relative importance of cross-flow (*CF*) modes compared to the most amplified *TS*-waves in the present configuration and to identify the *CF*-vortex with the strongest linear amplification. The investigation of the flow field in Fig. 4(b) yielded a well developed cross-flow component for higher sweep angles, which manifests itself in the increasing amplification of steady and unsteady cross-flow modes visible in the stability diagrams of Fig. 7. Despite the slightly weaker primary amplification rates observable in Fig. 7 the focus is here on steady *CF*-vortices, as they are well known to dominate unsteady *CF*-waves in low-turbulence environments like free flight as discussed by Deyhle and Bippes [37] or Wassermann and Kloker [38]. As the *CF*-amplification for the smaller sweep angles is too weak compared to the *TS*-waves to make them a relevant partner in mixed transition scenarios, we can constrain ourself to the 45°-separation bubble.

Local *LST*-investigations of the 45°-case compiled in Table 3 show that *CF*-vortices are first amplified at about $x = 1.4$ and thus later than *TS*-waves, but that they afterwards experience a rapid increase in their amplification rates to values of 30% to 40% of the most amplified *TS*-wave within the separation bubble. An evaluation of *CF*-vortices with *PSE*, which was found to be significantly more accurate for *CF*-vortices than *LST* in comparisons to *DNS*-results in by the authors [40], yielded the strongest overall amplification for the *CF*-vortex (0/50). Up to the middle of the separation bubble its initial amplitude approximately triples as demonstrated in Fig. 8(b) in comparison with the most amplified 45°-*TS*-wave, which grows three orders of magnitude.

5. Discussion and conclusions

The effect of sweep on the linear stability of a series of small, pressure-induced laminar separation bubbles on a swept infinite flat plate has been investigated systematically. To this end, the

DNS-base flow was evaluated for a range of sweep angles $\Psi_\infty = 0°, 15°, 30°, 45°$ by means of linear stability theory (*LST*) and solutions of the linear parabolised stability equations (*PSE*). The assumed homogeneity in span in combination with simplifications arising from studying steady laminar separation bubbles allowed for a comprehensive analysis of the influence of sweep on the structure and stability of such bubbles that would be hard to achieve for the complicated unsteady motion in the vicinity of an unsteady transitional separation bubble on finite wings.

Due to the independence principle of incompressible flow the laminar flow field may be obtained for arbitrary sweep angles Ψ_∞ by scaling the three-dimensional part of the generic 45°-solution with $\tan(\Psi_\infty)$, while leaving flow quantities already present in the unswept case unchanged. Therefore, the separation bubble series exhibits identical chordwise cross-sections, which enabled direct comparisons that yielded the following:

- Despite the simple dependency of the base flow on the sweep angle, the linear disturbance amplification in such a flow cannot be deduced from a stability analysis of the 45°-case. Only disturbances with leading-edge parallel wave fronts, for which the three-dimensional linear stability equations simplify to the unswept case again, grow sweep angle independent. Thus, each sweep angle constitutes a unique case in general.
  However, this does not imply that the differences in the growth rates of a particular mode in base flows with different sweep angles or of modes with similar frequencies and spanwise wavenumbers in the same base flow are large. Therefore, these findings do not constitute a contradiction to the approximate sweep angle independence of the time mean of the transitional separation bubbles of Kaltenbach and Janke [21], who observed a similar disturbance growth for the most amplified shear layer mode for sweep angles between 0° and 40° (see Fig. 17 there), qualitatively comparable to Fig. 8(b) in the present study. Consequently, the 40°-bubble in [21] shortens, but its length, which shows the integrated effect of all local differences, differs from the unswept case only moderately by 4% to 16%, depending on the initial disturbance spectrum.
- Investigations concerning the influence of sweep on the local stability of the separation bubble series showed that maximal linear amplification shifts monotonously towards disturbances (ω/γ) with higher frequencies ω and larger spanwise wave numbers γ with increasing sweep angle. Simultaneously, the spanwise wavenumbers γ_s in the streamline-oriented coordinate system are negative and monotonously decreasing. These modes exhibit propagation directions of roughly $-10°$ with respect to the local free-stream direction. Thus, oblique, left-running *TS*-waves, not *CF*-vortices, experience the strongest amplification even for high sweep angles. Compared to the unswept case, maximal amplification rates in the front part of the bubble increase in the order of 8% for $\Psi_\infty = 45°$.
- The influence of sweep on the amplitude of the most amplified *TS*-wave is moderate compared to the strong general amplification of three orders of magnitude in the separated shear layer: growth from the neutral point to the middle of the present separation bubble is about twice as strong for the 45°-case compared to the unswept case, a difference of less than one *N*-factor unit. Much as in attached swept boundary layers strongest linear growth for each sweep angle occurs for oblique *TS*-waves close to the free-stream direction Ψ_e. The typical deviation of the left-running waves to Ψ_e was about $-5°$.
  The same qualitative trend of *higher linear amplification for higher sweep angles* for oblique *TS*-waves with propagation angles smaller than the free stream direction was observed by Kaltenbach and Janke [21] in their study of transitional separation bubbles behind a backward facing step, though the influence was only weak in their case. No indication of maximal amplification in another direction then Ψ_e was found in the present base flow series though, as opposed to the "effective shear direction" of [21] with a substantial and increasing discrepancy to Ψ_e for a rising sweep angle. This emphasises again the differences between free shear layers and the wall bounded separated shear layers of pressure induced separation bubbles.
- Despite relevant cross-flow (*CF*) levels of up to about 9% of the local streamline free-stream velocity $u_{s,e}$ in the front part of the 45°-separation bubble, *CF*-influences on the present separation bubble series are weak, so that only the highest sweep angle of $\Psi_\infty = 45°$ was studied. There, steady cross-flow vortices reached local growth rates in the order of 30% of the most amplified *TS*-waves. The most amplified *CF*-vortex triples its amplitude from the neutral point to the middle of the separation bubble, while the corresponding *TS*-waves grows three orders of magnitude. Therefore, steady *CF*-vortices can only be relevant for the transition process in the given configuration, if they reach the non-linear regime or if their amplitudes are significantly higher than that of the *TS*-waves in the initial disturbance spectrum.
  For the interpretation of these results, however, the reader should keep in mind that the favourable pressure gradient region encountered in front of midchord bubbles on swept infinite wings was not modelled here as discussed in Section 2 and that thus the results are not directly transferable to the situation on swept infinite wings. Furthermore, the subject of receptivity is beyond linear analysis and wall roughness is known to be very efficient in exciting steady cross flow vortices in low-turbulence level-environments as under free flight conditions, so that high amplitudes levels of *CF*-vortices are likely to be encountered on wings. Following a similar discussion of Wassermann and Kloker [38] for attached boundary layer flow, one could argue this is indeed the main feature of the most likely transition scenario in connection with *TS*-*CF*-interactions in midchord bubbles on swept wings. If transition did not already occur in the favourable pressure gradient (FPG) region, steady *CF*-vortices of considerable amplitudes, but below the critical threshold for secondary flow instability, can be expected to be convected into the adverse pressure gradient region of the separation bubble.

Regarding the base flow structure, the independence principle leads to a quasi-two-dimensional flow field, where the spanwise flow is superimposed over the unchanging chordwise cross-section of the separation bubble. The investigation showed that this results in a relevant spanwise velocity component inside. It reaches up to about 10% of the chordwise inflow velocity U_∞ in the middle of the present 45°-separation bubble, a value that scales with $\tan(\Psi_\infty)$ for smaller sweep angles Ψ_∞ due to (7). Therefore, the term "dead-air region", coined for the often very weak backflow under the separated shear layer in the front part of unswept separation bubbles, becomes less accurate with increasing sweep angle. For the same reason the total wall shear stress along the separation line becomes positive throughout, while it vanishes in the unswept case. This is consistent with findings of Horton [2] for swept transitional bubbles, who concluded that "cordwise velocities are negligibly small, whilst small spanwise velocities are apparent" in this region.

Acknowledgements

The authors would like to thank the DLR-Göttingen for the permission to use their linear NOLOT-PSE-code and especially Dr. Hein

for his able support when we started working with it. The financial support by the Deutsche Forschungsgemeinschaft (DFG) under contract number Ri 680/12-1 is gratefully acknowledged.

References

[1] M. Gaster, On the stability of parallel flows and the behaviour of separation bubbles, PhD thesis, Queen Mary College, University of London, 1963.
[2] H. Horton, Laminar separation bubbles in two and three dimensional incompressible flow, PhD thesis, Department of Aeronautical Engineering, Queen Mary College, University of London, 1968.
[3] W.R. Briley, A numerical study of laminar separation bubbles using the Navier–Stokes equations, J. Fluid Mech. 47 (1971) 713–736.
[4] I.P. Castro, The stability of laminar symmetric separated wakes, J. Fluid Mech. 532 (2005) 389–411.
[5] F. Bao, Experimental investigations of transitional unsteady separated vortex flows, PhD thesis, Faculty of Mechanical Engineering, Universität Hannover, 2001. Also published as: Inst. Aerodynamics and Flow Technology, DLR-Göttingen, Tech. Rep. DLR-2001-20.
[6] A. Michalke, On the inviscid instability of wall-bounded velocity profiles close to separation, ZFW 14 (1990) 24–31.
[7] M. Gaster, Stability of velocity profiles with reverse flow, in: M.Y. Hussaini, A. Kumar, C.L. Streett (Eds.), Instability, Transition and Turbulence, ICASE-Workshop, Springer-Verlag, Berlin, 1991, pp. 212–215.
[8] T. Allen, N. Riley, Absolute and convective instabilities in separation bubbles, Aeron. J. Roy. Aeron. Soc. 99 (1995) 439–448.
[9] D.A. Hammond, L.G. Redekopp, Local and global instability properties of separation bubbles, Eur. J. Mech. B/Fluids 17 (1998) 145–164.
[10] M. Alam, N.D. Sandham, Direct numerical simulation of 'short' laminar separation bubbles with turbulent reattachment, J. Fluid Mech. 403 (2000) 223–250.
[11] U. Rist, U. Maucher, Investigations of time-growing instabilities in laminar separation bubbles, Eur. J. Mech. B/Fluids 21 (2002) 495–509.
[12] O. Marxen, M. Lang, S. Wagner, A combined experimental/numerical study of unsteady phenomena in a laminar separation bubble, Flow, Turbulence and Combustion 71 (2003) 133–146.
[13] V. Theofilis, Advances in global linear instability analysis of nonparallel and three-dimensional flows, Progr. Aerospace Sci. 39 (2003) 249–315.
[14] M. Marquille, U. Ehrenstein, On the onset of nonlinear oscillations in a separating boundary-layer flow, J. Fluid Mech. 490 (2003) 169–188.
[15] F. Alizard, J.-Ch. Robinet, Spatially convective global modes in a boundary layer, Phys. Fluids 19 (2007) 105–114.
[16] O. Marquet, D. Sipp, J.-M. Chomaz, L. Jacquin, Amplifier and resonator dynamics of a low-Reynolds-number recirculation bubble in a global framework, J. Fluid Mech. 605 (2008) 429–443.
[17] E. Akervik, U. Ehrenstein, F. Gallaire, D.S. Henningson, Global two-dimensional stability measures of the flat plate boundary-layer flow, Eur. J. Mech. B/Fluids 27 (5) (2008) 501–513.
[18] E. Greff, In-flight measurements of static pressures and boundary-layer state with integrated sensors, J. Aircraft 28 (1991) 289–299.
[19] T. Hetsch, U. Rist, An analysis of the structure of laminar separation bubbles in swept infinite geometries, Eur. J. Mech. B/Fluids 28 (4) (2009) 486–493.
[20] A.D. Young, H.P. Horton, Some results of investigations of separation bubbles, AGARD CP No. 4, 1966, pp. 780–811.
[21] H.-J. Kaltenbach, G. Janke, Direct numerical simulation of a flow separation behind a swept, rearward-facing step at $Re_H = 3000$, Phys. Fluids 12 (2000) 2320–2337.
[22] H.-J. Kaltenbach, The effect of sweep-angle variation on the turbulence structure in a separated, three-dimensional flow, Theoret. Comput. Fluid Dynamics 16 (2003) 187–210.
[23] W. Jürgens, H.-J. Kaltenbach, Eigenmode decomposition of turbulent velocity fields behind a swept, backward-facing step, J. Turbulence 4 (2003) 1–21.
[24] G. Lu, S. Lele, Inviscid instability of a skewed compressible mixing layer, J. Fluid Mech. 249 (1993) 441–463.
[25] A.V. Dovgal, V.V. Kozlov, A. Michalke, Laminar boundary layer separation: Instability and associated phenomena, Progr. Aerospace Sci. 30 (1994) 61–94.
[26] U. Rist, Zur Instabilität und Transition laminarer Ablöseblasen, Habilitation, Universität Stuttgart, Shaker, 1999.
[27] U. Rist, U. Maucher, S. Wagner, Direct numerical simulation of some fundamental problems related to transition in laminar separation bubbles, in: J.-A. Désidéri, C. Hirsch, P. Le Tallec, M. Pandolfi, J. Périaux (Eds.), Computational Fluid Dynamics '96, John Wiley & Sons, Ltd., 1996, pp. 319–325.
[28] U. Rist, H.F. Fasel, Direct numerical simulation of controlled transition in a flat-plate boundary layer, J. Fluid Mech. 298 (1995) 211–248.
[29] S. Bake, D.G.W. Meyer, U. Rist, Turbulence mechanisms in Klebanoff transition: A quantitative comparison of experiment and direct numerical simulation, J. Fluid Mech. 459 (2002) 217–243.
[30] P. Wassermann, M. Kloker, Mechanisms and passive control of crossflow-vortex-induced transition in a three-dimensional boundary layer, J. Fluid Mech. 456 (2002) 49–84.
[31] T. Hetsch, U. Rist, On the structure and stability of three-dimensional laminar separation bubbles on a swept plate, in: C. Breitsamter, B. Laschka, H.J. Heinemann, R. Hilbig (Eds.), Proc. 13. DGLR/STAB-Symposium, NNFM 87, Munich, Germany 2002, Springer, 2004, pp. 302–310.
[32] T. Hetsch, U. Rist, The effect of sweep on laminar separation bubbles, in: R. Govindarajan (Ed.), Sixth IUTAM Symposium on Laminar-Turbulent Transition, Proc. IUTAM-Symp., Bangalore, India, December 2004, in: Fluid Mechanics and Its Applications, vol. 78, Springer, 2006, pp. 395–400.
[33] T. Hetsch, U. Rist, Direct numerical simulation and analysis of the flow field around a swept laminar separation bubble, in: W. Nagel, W. Jäger, M. Resch (Eds.), High Performance Computing in Science and Engineering '06, Springer, 2007, pp. 205–221.
[34] S. Hein, Linear and nonlinear nonlocal instability analyses for two-dimensional laminar separation bubbles, in: H.F. Fasel, W.S. Saric (Eds.), Laminar-Turbulent Transition, Proc. IUTAM Symp. on Laminar-Turbulent Transition, Sedona, USA, September 13–17, 1999, Springer, 2000, pp. 681–686.
[35] V.G. Chernoray, A.A. Bakchino, V.V. Kozlov, L. Löfdahl, Experimental study of the K-regime of breakdown in straight and swept wing boundary layers, Phys. Fluids 13 (2001) 2129–2132.
[36] U. Rist, U. Maucher, Direct numerical simulation of 2-D and 3-D instability waves in a laminar separation bubble, in: AGARD-CP-551, Application of Direct and Large Eddy Simulation to Transition and Turbulence, 1994, pp. 34-1–34-7.
[37] H. Deyhle, H. Bippes, Disturbance growth in an unstable three-dimensional boundary layer and its dependence on environmental conditions, J. Fluid Mech. 316 (1966) 73–113.
[38] P. Wassermann, M. Kloker, Transition mechanisms in a three-dimensional boundary layer flow with pressure-gradient changeover, J. Fluid Mech. 530 (2005) 265–293.
[39] L. Prandtl, K. Oswatitsch, K. Wieghardt, Führer durch die Ströungslehre, 9 Edition, Vieweg, 1990.
[40] T. Hetsch U. Rist On the accuracy of local and nonlocal linear stability theory in swept laminar separation bubbles, AIAA Journal, in press.